Mask pattern interference in AlGaInAs selective area metal-organic vapor-phase epitaxy: Experimental and modeling analysis

N. Dupuis,[1,a)] J. Décobert,[1] P.-Y. Lagrée,[2] N. Lagay,[1] F. Poingt,[1] C. Kazmierski,[1] A. Ramdane,[3] and A. Ougazzaden[4]

[1]*Alcatel Thales III-V Lab., Route de Nozay, F-91461 Marcoussis, France*
[2]*CNRS, UPMC Univ Paris 06, IJLRA, F-75005, Paris, France*
[3]*CNRS LPN, Route de Nozay, 91460 Marcoussis, France*
[4]*Georgia Tech - CNRS , 2 rue Marconi, 57070, Metz, France*

We studied selective area growth modeling and characterization of the AlGaInAs material system. We used a three-dimensional vapor phase diffusion model to extract the effective diffusion lengths of Al, Ga, and In species from measured thickness profiles of the three binaries AlAs, GaAs, and InP. Our growth conditions yield to 50, 85, and 10 μm for Al, Ga, and In, respectively. Based on these values, we achieved a precise prediction of AlGaInAs thickness, composition, band gap, and biaxial strain variations in different selective area growth conditions. Particular attention was paid to the influence of neighboring cells in the case of high mask density. This configuration occurs in practical component mask layout. High mask density leads to interferences between masked cells and enhances the effect of the long diffusion length of aluminum and gallium species. Then, the biaxial strain is tensile shifted and the band gap is blue shifted in the vicinity of a mask, compared to reference material features grown away from the mask. High-resolution micro-photoluminescence and optical interferometer microscopy measurements confirmed the validity of simulated band gap and thickness variations for both bulk and multi-quantum well layers. © *2008 American Institute of Physics*. [DOI: 10.1063/1.2937167]

I. INTRODUCTION

Selective area growth (SAG) attracts considerable interest as a powerful tool for monolithic integration of active and passive photonic functions, opening the way to the achievement of reduced cost InP-based photonic integrated circuits. With this technology, different band gap materials can be defined simultaneously in a single epitaxial growth, thereby leading to well-controlled simplified processing in comparison with etch-regrowth-based methods such as the butt-joint technique.[1] SAG is based on metallorganic vapor phase epitaxy (MOVPE) on dielectric patterned substrates. Provided the active precursors do not nucleate on dielectric amorphous surfaces, they diffuse and induce a growth rate enhancement in the vicinity of the masked zone. In the case of ternary or quaternary alloys, the mask induces a spatial compositional shift due to the different decomposition and diffusion rates of group III element precursors in the vapor phase. This shift produces a band-gap variation around the mask, especially in the case of multi-quantum well (MQW) structures where the electronic transitions also depend on the well's thickness. An appropriate design of the mask pattern then allows integration of different band-gap areas on the same wafer. For example, an integration of an active and passive waveguides such as a spot size converter with both thickness and refractive index tapering[2] is possible, allowing expansion of the optical mode and hence, reduction of the component to optical fiber coupling losses. The SAG technique has been used by many research groups in different integration schemes.

Examples of such integrations are distributed feedback laser/electroabsorption modulator (EAM),[3] integrated tunable distributed Bragg reflector laser/EAM,[4] semiconductor optical amplifier/EAM,[5,6] or more complex devices such as selectable wavelength light sources for dense wavelength division multiplexing.[7]

In order to realize and control complex monolithic integrations with SAG band-gap engineering, we report here on the development of a predictive modeling tool. This work was carried out in two steps. First, we built a two-dimensional model which calculates material thickness across infinite dielectric stripes. This model has been used to determine the effective diffusion lengths of different species corresponding to specific growth conditions. This was achieved by fitting experimental thickness values for simple binary materials. Second, the knowledge of effective diffusion lengths was used to develop a three-dimensional model suitable for the simulation of SAG growth (thickness, composition, wavelength, strain) around an arbitrary mask shape. In practical component fabrication masks a periodic layout is often adopted where each mask pattern is surrounded by identical neighbors that may influence SAG. These proximity effects, also called interference effects,[8] have to be taken into account in the component design and have thus been included in our model. Our primary interest was focused on the AlGaInAs material system which has a growing industrial importance for the new generation of low-cost telecommunication components. This is due to a large conduction/valence band discontinuity split ($\Delta Ec / \Delta Eg \approx 0.7$), resulting in a high electron confinement which leads to improved gain, absorption, and dynamic and thermal characteristics of components.
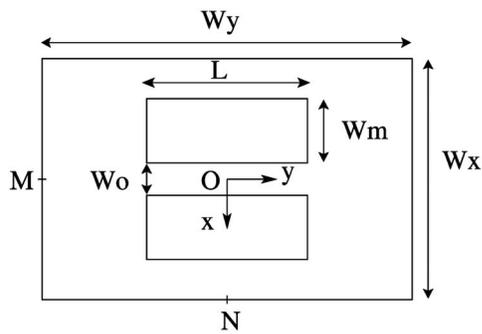
a)Electronic mail: nicolas.dupuis@3-5lab.fr.

FIG. 1. Schematic of the growth pattern with the dimensions *Wm*, *Wo*, *L*, *Wx*, and *Wy*. Three points are also marked: $O(0,0)$, $M(0,-Wy/2)$, and $N(Wx/2,0)$.

However, compared with the standard GaInAsP material system which has been widely investigated by SAG,[9–14] only few reports deal with the AlGaInAs alloys.[15–18]

Here, binaries, ternaries, and quaternaries of the AlGaInAs material system were selectively grown and their characteristics systematically compared. Details on the growth conditions and characterization results are developed in Sec. II. Section III introduces the governing equations and boundaries of the vapor phase diffusion model and then explains the periodicity of the computed SAG cell. In Sec. IV we present the effective diffusion length extraction of Al, Ga, and In species in our growth conditions. Section V is devoted to the predictive modeling of ternary and quaternary AlGaInAs alloys. This includes the calculation of thickness enhancement and compositional variations. The influence from nearest neighbors in a periodic SAG cell is also investigated with a specifically designed mask layout. In the last section, an actual integration case is reported with an AlGaInAs MQW structure selectively grown on a periodic mask with a high cell density.

II. EXPERIMENTAL

All investigated samples were grown in a horizontal AIX200/4 MOVPE reactor, designed for three 2 in. wafers, using trimethylaluminum (TMAl), trimethylgallium (TMGa), trimethylindium (TMIn), arsine (AsH$_3$), and phosphine (PH$_3$) as growth precursors.[19] Bulk layers including InP, InAs, GaAs, AlAs binary, AlInAs, GaInAs, GaAlAs ternary, AlGaInAs quaternary alloys, and AlGaInAs MQW structures were selectively grown in lattice-matched conditions on various InP, InAs, and GaAs (001) appropriately patterned substrates. The SiO$_2$ mask stripes were processed using conventional photolithography and reactive ion etching. The mask pattern consists of two parallel dielectric stripes aligned along the [110] crystallographic direction. The cell geometry (Fig. 1) is defined by the stripe length (*L*), the stripe width (*Wm*), and the opening width (*Wo*) between two stripes. *Wx* and *Wy* define the free area size around the two stripes that are reproduced periodically from cell to cell. Three masks were used in this study. All the dimensions will be quantified later in the paper.

(i) The first mask, named A, is used for the parametrical study. *L*, *Wx*, and *Wy* are kept constant and are large com-

pared with *Wo* and *Wm*, which vary monotonously. Therefore, the different patterns are sufficiently separated to avoid any influence on each other.

(ii) The second mask, named B, is for the periodicity study. *Wm*, *Wo*, and *L* are kept constant. *Wx* and *Wy* are changed to evaluate the interference between the nearest-neighbor patterns.

(iii) The third mask, named C, is used for our optoelectronic device integration. The density of integration is high and the stripes are very long compared to *Wm* and *Wo*.

The growth conditions for all samples are: temperature of 650 °C, pressure of 150 mbar, and nominal growth speed of 0.1 nm/s for binaries and 0.2 nm/s for ternaries and quaternaries. These conditions were optimized for AlGaInAs material growth on InP and have previously been reported.[20] In this study, they were kept constant for all alloys in order to fix the vapor phase diffusion lengths of species and therefore allow direct comparison and extrapolation between samples. The SiO$_2$ dielectric mask led to a perfect selectivity (i.e., no polycrystalline deposition on the mask) for all mask widths and for all samples, including the more aluminum-rich ones (e.g., AlAs). For each sample, thickness enhancement and overgrowth near the mask were characterized by optical interferometer microscopy (OIM) with a high vertical resolution (± 5 nm). For ternary, quaternary alloys and MQW structures, the emission spectra were measured by microphotoluminescence (μ-PL) at room temperature with a 680 nm laser diode providing a spot size of $2-3$ μm. In the field region (i.e., far away from the masked areas) high resolution x-ray diffraction (HRXRD) measurements were used to obtain the amount of lattice mismatch for ternary and quaternary alloys as well as for the MQW stack.

III. VAPOR-PHASE DIFFUSION MODEL

AlGaInAs alloys have three group III elements (Al, Ga, and In) for only one group V element (As). The organometallic precursors for these elements provide different vapor and surface decomposition rates and different diffusion coefficients in the vapor phase. In conventional epitaxy, these differences are not important as any desired AlGaInAs composition can be achieved by an adjustment of the precursor flow. In SAG, as the precursors cannot react on the mask, extra material is available over the masked zone and a lateral concentration gradient builds-up. This gradient leads to extra lateral diffusion of species around the mask and to a local enhancement of the growth rate. Thus, in the SAG regime, diffusion rates and surface reaction rates of Al, Ga, and In precursors become measurable. This is especially true with ternary and quaternary alloys where spatial compositional variation occurs around the mask.

A simple approach to model the selective growth regime is to consider only vapor phase diffusion (VPD) as the source of material supply.[12,13] This assumes a laminar flow, the existence of a stagnant layer in contact with the wafer surface, and the absence of deposition on mask surface. The molecules diffuse and are incorporated onto the exposed crystal surface. Surface diffusion on the mask is ignored in the present model since it occurs within only a few micrometers
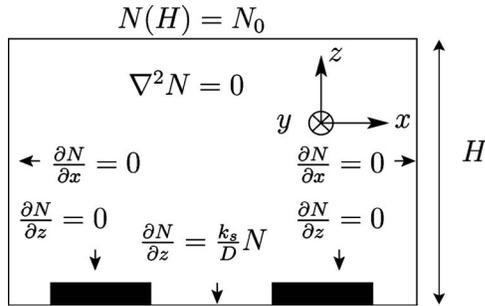
$$N(H) = N_0$$
$$\nabla^2 N = 0$$
$$\frac{\partial N}{\partial x} = 0 \qquad \frac{\partial N}{\partial x} = 0$$
$$\frac{\partial N}{\partial z} = 0 \qquad \frac{\partial N}{\partial z} = \frac{k_s}{D} N \qquad \frac{\partial N}{\partial z} = 0$$

FIG. 2. Schematic of the periodic window calculation with governing equations and boundary conditions.

of the dielectric edge.[12,13] The Laplace equation of the concentration $\nabla^2 N=0$ is solved in three dimensions with specific boundary conditions[12,13] (see Fig. 2). On the mask, as no species are incorporated, the flux is equal to 0, hence $(\partial N / \partial z)_{z=0}=0$. On the crystal, the Langmuir isotherm-like condition $D(\partial N / \partial z)_{z=0}=k_s N$ is assumed with D being the diffusion coefficient of the reactants in the vapor phase and k_s a sticking rate constant which depends on the reactivity of source molecules on the crystal surface. At the top of the stagnant layer (H), the concentration is assumed constant $N(H)=N_0$ (i.e., infinite diffusion source). Finally, the periodicity of the domain leads to $(\partial N / \partial x)_{z=0}=0$ for left and right boundaries. These boundary conditions are depicted in Fig. 2. Note that without any mask, the solution is linear in z and we readily obtain

$$N(z) = N_0 \frac{\frac{k_s z}{D} + 1}{\frac{k_s H}{D} + 1}. \tag{1}$$

To solve the full problem, we investigated several numerical approaches: finite differences, finite elements, and fast Fourier transform (FFT). In each case, the numerical results were identical. In practice, results presented in the following were obtained using the FFT method. To implement this last method we worked on

$$n(x,y) = \int \int \hat{n}(k_x,k_y)e^{i(k_x dx + k_y dy)}dk_x dk_y, \tag{2}$$

which represents the perturbation from the equilibrium concentration Eq. (1) induced by the mask where k_x and k_y are the Fourier modes. The effective concentration on the crystal surface is then

$$N^{\text{eff}}(x,y) = N(0) + n(x,y). \tag{3}$$

The latter concentration profile strongly depends on the geometrical dimensions Wm and Wo. The dimensions of the calculation window (Wx and Wy) define the periodicity of the domain which is natural in the FFT method: in the calculation the cell in Fig. 1 is assumed to be surrounded by identical cells with the same dimensions Wx and Wy. These close cells actually play an important role as they will interfere with each other. This periodicity is fundamental to model the SAG process, especially for device integration, where a large number of closely spaced components is usu-

ally desired. Inherent to the FFT method is the problem of the Fourier modes $k_x=0$ and $k_y=0$, which are solved by applying the Green–Ostrogradsky formula on the calculation domain.

In the following discussion, we will consider the normalized concentration R also named growth rate enhancement,

$$R(x,y) = \frac{N^{\text{eff}}(x,y)}{N(0)}. \tag{4}$$

The main advantage of the VPD approach is to give a simple way to determine the effective diffusion length (D/k_s parameter) which is, apart from the geometrical dimensions of the mask, the only adjustable parameter of the model.

IV. BINARY COMPOUNDS: AL, GA, AND IN (D/k_s) EXTRACTION

In the case of AlGaInAs alloys, three effective diffusion lengths are considered: $(D/k_s)_{\text{Al}}$, $(D/k_s)_{\text{Ga}}$, and $(D/k_s)_{\text{In}}$. The approach proposed here to determine these parameters is a fitting between OIM thickness measurements of the binary alloys (AlAs, GaAs, and InAs) and VPD calculations on mask A. A precise adjustment between the calculated and experimental thickness profiles leads to the (D/k_s) parameter for each binary. In the case of $(D/k_s)_{\text{In}}$ extraction, both InAs and InP binaries were considered. We observed that InAs exhibits a slightly higher growth rate enhancement than InP. This small difference was already mentioned by Caneau *et al.*[9] who studied the effect of group V elements for different binaries (InAs, InP, GaAs, GaP). They explained that the decomposition rate of TMIn (or TMGa) precursor is enhanced in the presence of AsH$_3$ compared to PH$_3$. However, the difference is quite small and the influence on $(D/k_s)_{\text{In}}$ is negligible. The fit was actually done with InP because of perturbed morphology in the case of InAs growth. We believe this problem arises from the fixed growth temperature chosen for our study (T=650 °C), which is too high for InAs. Figure 3 shows the fit for the three binary compounds along the x direction ($y=0$) for two mask widths, $Wm=80$ and 120 μm, and with $Wo=30$ μm. The experimental thickness was measured using the OIM setup and normalized relatively to the field reference in order to deduce the experimental growth rate enhancement (GRE) ratios R_{AlAs}, R_{GaAs}, and R_{InP}. In the following, these ratios are noted R_{Al}, R_{Ga}, and R_{In} in order to simplify notations. From these results the three extracted diffusion lengths in our growth conditions are $(D/k_s)_{\text{Al}}=50$ μm, $(D/k_s)_{\text{Ga}}=85$ μm, and $(D/k_s)_{\text{In}}=10$ μm. The indium and gallium values are in qualitative agreement with those already reported in the literature.[12–15] The aluminum one is found intermediate between indium and gallium ones. This value for aluminum is clearly confirmed in Fig. 3. Indeed, in the vicinity of the mask, the slope of the AlAs thickness enhancement profile (a) appears steeper than the GaAs one (b). The extracted (D/k_s) parameters control the thickness enhancement profile in the vicinity of a selective mask for the three binaries. They also appear as key parameters in predictive modeling of thickness and compositional
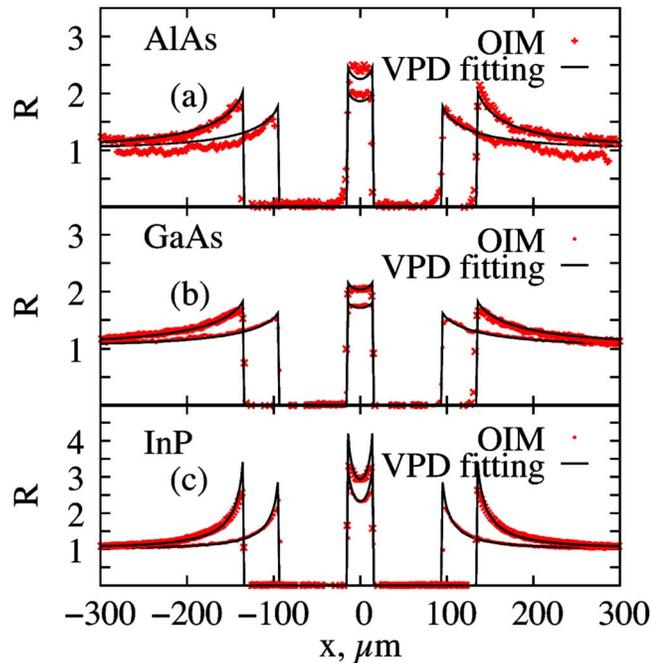
FIG. 3. (Color online) Binary fitting (mask A) with VPD model along the x direction ($y=0$): (a) AlAs($D/k_s=50$ μm), (b) GaAs($D/k_s=85$ μm), and (c) InP($D/k_s=10$ μm). The fittings are repeated for two mask widths, $Wm=80$ and 120 μm. L, Wx, and Wy are kept constant: $L=800$ μm, $Wo=30$ μm, $Wx=900$ μm, and $Wy=1400$ μm.

variations for ternary and quaternary alloys. In the next section, we show that this modeling can be based on simple linear relations between binaries results.

V. TERNARY AND QUATERNARY ALLOYS

Selective growth modeling of ternary and quaternary alloys is more complex since two or three group III elements are mixed in the vapor phase. The simplest model is to assume no interaction between III elements and a linear dependence of the alloy GRE ratio (denoted R_a) with the binary GRE (R_{Al}, R_{Ga}, and R_{In}).[21] For quaternary alloys, the notation $Al_\alpha Ga_\beta In_{1-\alpha-\beta}As$ is adopted in the text. The group III element compositional ratios (α, β, and $1-\alpha-\beta$) depend on the position (x,y) in the cell. For ternary alloys, one of these ratios is simply equal to zero. In the field region the quaternary reference composition is written: $Al_{\alpha_r}Ga_{\beta_r}In_{1-\alpha_r-\beta_r}As$. This reference composition can be fully characterized with HRXRD and photoluminescence (PL) on an unmasked reference sample. For a ternary or quaternary alloy with (α_r, β_r) reference composition, the growth rate enhancement $R_a(x,y)$ can be written as

$$R_a(x,y) = \alpha_r R_{Al}(x,y) + \beta_r R_{Ga}(x,y)$$
$$+ (1 - \alpha_r - \beta_r)R_{In}(x,y), \qquad (5)$$

and the compositional ratio $C_e(x,y)$ of the e element (e=Al, Ga, In when $i=\alpha$, β, $1-\alpha-\beta$, respectively) is

$$C_e(x,y) = \frac{i_r R_e(x,y)}{R_a(x,y)}, \qquad (6)$$

where R_e denotes the GRE for element e. In order to obtain AlGaInAs $R_a(x,y)$ and $C_e(x,y)$, the FFT numerical calcula-
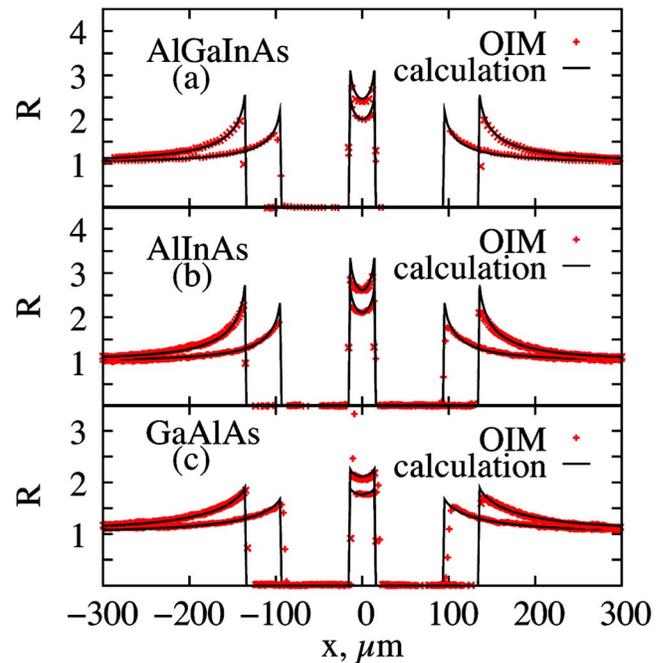

FIG. 4. (Color online) Growth rate enhancement (R) in VPD modeling and OIM measurements (mask A) along the x direction ($y=0$) for quaternary and ternary alloys: (a) AlGaInAs with $\alpha_r=0.114$ and $\beta_r=0.440$, (b) AlInAs with $\alpha_r=0.519$ and $\beta_r=0$, and (c) GaAlAs with $\alpha_r=0.260$ and $\beta_r=0.740$. The calculations are repeated for two mask widths, $Wm=80$ and 120 μm. L, Wo, Wx, and Wy are kept constant: $L=800$ μm, $Wo=30$ μm, $Wx=900$ μm, and $Wy=1200$ μm.

tion is repeated three times with the three diffusion lengths determined in the last section, to obtain $R_{Al}(x,y)$, $R_{Ga}(x,y)$, and $R_{In}(x,y)$ independently. The variations of band gap, biaxial strain, and electronic transitions are deduced from Eqs. (5) and (6).

From a theoretical point of view, these equations lead to some useful comments. First, in the case of a quaternary alloy with three group III elements such as AlGaInAs and when varying Wm, if the compositional ratio of one element remains practically unchanged, this implies that the corresponding species has an intermediate diffusion length value to the two other species. This is typically the case for aluminum. The interpretation is quite different in the case of the two group V elements of a quaternary alloy such as GaInAsP for which both As and P species have very large diffusion lengths, and the compositional ratio between As and P is constant.[12] Second, we can also notice that in the AlGaInAs well and barrier heterostructures, the growth rate enhancement R_{a-well} and $R_{a-barrier}$ can be very different since α_r, β_r, and $1-\alpha_r-\beta_r$ are different for well and barrier compositions.

A. Thickness enhancement

Thickness enhancement of ternary and quaternary alloys is successfully predicted with the simple linear approach described by Eq. (5). This equation uses the (D/k_s) value previously extracted from the binary alloys without any adjustment . Figure 4 shows an example for AlGaInAs quaternary (a) and AlInAs (b), GaAlAs (c) ternary alloys. The calculated GRE remarkably fit the OIM measured profiles (mask A). The reference compositions (α_r, β_r) were deduced from
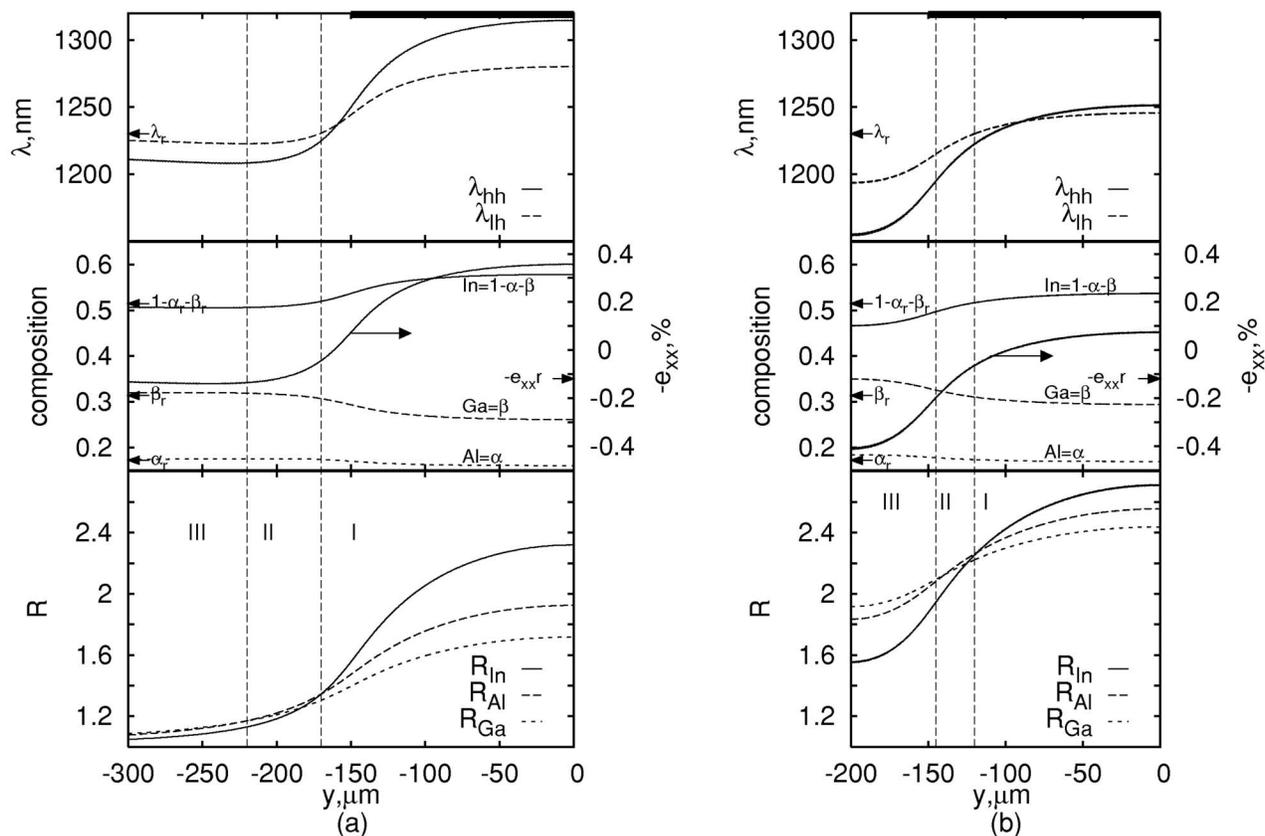
FIG. 5. From bottom to top, calculated growth rate enhancement R for binaries, compositional variations (left axis)/biaxial strain $-e_{xx}$ (right axis), and material wavelength variation for the heavy (λ_{hh}) and light hole bands (λ_{lh}) for an AlGaInAs quaternary with $\alpha_r=0.172$ and $\beta_r=0.313$ along the y direction (at $x=0$): (a) $Wx=Wy=1000\ \mu m$, graphs only plotted on $[-300;0]$; (b) $Wx=Wy=400\ \mu m$. In both cases $Wm=140\ \mu m$, $Wo=40\ \mu m$, and $L=300\ \mu m$. A bold trace sketches the position of the selective mask.

HRXRD characterization for ternaries and from a combination of PL and HRXRD for the quaternary. As seen from these results, the simple approach of the linear model of the growth rate enhancement, as suggested by Eq. (5), appears quite appropriate. A comparison between $R_a(x,y)$ of GaAlAs from Fig. 4(c), and $R_{Al}(x,y)$ and $R_{Ga}(x,y)$ from Figs. 3(a) and 3(b) clearly shows that for the same mask pattern, the sharpness of the GaAlAs profile is intermediate between those of GaAs and AlAs. This gives weight to the arguments discussed in the previous section concerning the value of $(D/k_s)_{Al}$.

B. Compositional variations and mask pattern interference

The compositional ratios (α=Al, β=Ga, and $1-\alpha-\beta$=In) display very different values depending on the mask geometry (Wm, Wo, and L), the position (x,y) in the cell, and the dimensions of the cell (Wx and Wy). As expected, the indium species, which has the shortest effective diffusion length, highly enriches in the near vicinity of the mask. On the other hand, the other elements, aluminum and gallium, have an influence which extends further from the mask edge. Alam *et al.*[13] described a similar analysis in the GaInAsP material system. They compared the long-range effect of the gallium element compared to the indium shorter range. In the AlGaInAs material family, this longer range effect applies to both aluminum and gallium species. This effect is, however,

quite subtle to observe since the longer diffusion length of Al and Ga tends to homogenize their concentration distribution on a larger surface. Hence, their contribution to the alloy GRE (R_a) is generally lower than that of the indium precursor. With mask A, where Wx and Wy are large, this contribution is not observable since at the distance at which it occurs, the nominal growth rate is almost recovered (i.e., $R_a \approx 1$). However, with mask B and smaller Wx and Wy, the cells are influencing each other and the contributions of aluminum and gallium become detectable. This case is depicted in Fig. 5 through cross sections along the y direction (at $x=0$) for an AlGaInAs quaternary alloy with the following reference composition, $\alpha_r=0.172$ and $\beta_r=0.313$. In this figure, we present the simulated variations of binaries GRE (R_{Al}, R_{Ga}, and R_{In}), the compositional ratios [α, β, and $1-\alpha-\beta$ calculated with Eq. (6)], the biaxial strain $-e_{xx}$, and the emission wavelength corrected for the strain for heavy/light hole bands ($\lambda_{hh}/\lambda_{lh}$). The mask geometry is $Wm=140\ \mu m$, $Wo=40\ \mu m$, and $L=300\ \mu m$. Only a half mask is represented since the profile is symmetric. A bold trace on the (a) and (b) upper graphs shows the SiO$_2$ mask (y,z) cross section.

In the following, we compare the compositional enrichment variations with respect to different mask configurations. To help with this comparison, we arbitrarily define three zones denoted I, II, and III which correspond to indium, aluminum, and gallium highest GRE, respectively. In zone I,
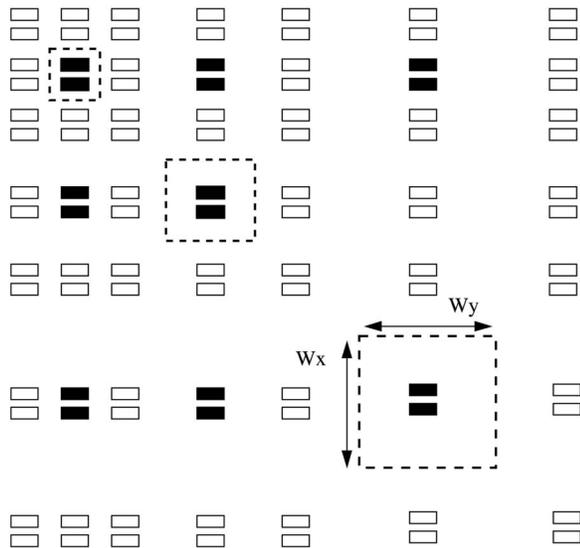
FIG. 6. Part of the mask B used for the periodicity measurements. On the figure, the cells respecting the periodicity criterion are filled. The characterized ones are surrounded by a dashed line.

FIG. 7. AlGaInAs quaternary (α_r=0.172 and β_r=0.313) measured (μ-PL) and calculated emission wavelength against $Wx=Wy$ for different points: $O(0,0)$, $M(0,-Wy/2)$, and $N(Wx/2,0)$. The reference wavelength is indicated by an arrow and is λ_r=1230 nm. Mask dimensions (mask B) are set to: Wm=140 μm, Wo=40 μm, and L=300 μm.

$R_{In}>R_{Al}$, R_{Ga}, in zone II, $R_{Al}>R_{Ga}$, R_{In}, and in zone III, $R_{Ga}>R_{In}$, R_{Al}. These three zones are separated in Fig. 5 by means of vertical dashed lines. Two calculated configurations are compared:

(i) In the first situation (a), Wx and Wy are large (Wx =Wy=1000 μm) and zone I extends over a large interval ($y\in[-170;0]$). In this zone, as seen on (a) middle graph left axis, an indium enrichment compared with the reference composition (see arrows on composition axis) is observed contrary to gallium and aluminum elements and, consequently, the biaxial strain $-e_{xx}$ (see middle graph right axis) shifts to compression. Therefore, the emission wavelength [upper (a) graph] is red shifted compared to the reference one (see arrow on wavelength axis). In zones II ($y\in[-220;-170]$) and III ($y\in[-300;-220]$), which are aluminum and gallium predominance areas, respectively, the nominal growth rate is almost recovered ($R_{In}\approx R_{Al}\approx R_{Ga}\approx R_a\approx 1.1$) and the small extra aluminum and gallium incorporation does not significantly affect the wavelength ($\lambda\approx\lambda_r$).

(ii) In the second situation (b), Wx and Wy are smaller ($Wx=Wy$=400 μm) and the influence between cells now plays a major role. In this case, the concentration profiles R_{Al}, R_{Ga}, and R_{In} are enhanced compared with the previous configuration; in addition, the indium predominance (zone I) is occurring over a smaller part. Zone I is extending to $y\in[-120;0]$ and, similar to the first configuration (a), the indium species concentration is enriched in this zone. Due to neighbor cell's influence, in the aluminum and gallium predominance zones (II and III), the nominal GRE is not recovered and a non-negligible aluminum and gallium enrichment is observed. Consequently, the biaxial strain is tensile shifted on the whole profile compared with situation (a). Moreover, in zones II ($y\in[-145;-120]$) and III ($y\in[-200;-145]$), a wavelength blue shift is observed: $\lambda<\lambda_r$.

In order to confirm these proximity effects, a specific SAG mask was designed and fabricated. A part of this mask is shown in Fig. 6. The purpose of this design was to have,
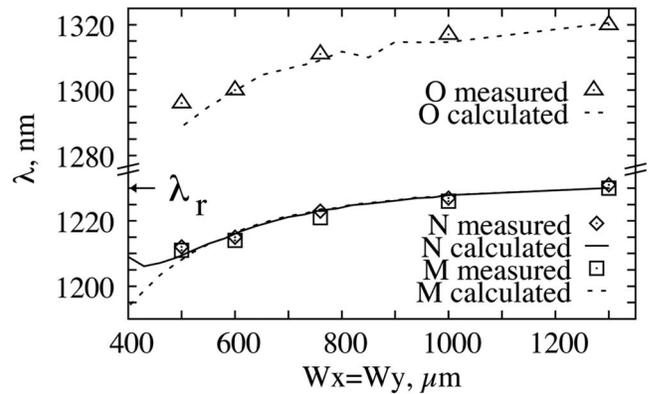
on the same sample, an identical mask pattern (Wm =140 μm, Wo=40 μm, and L=300 μm) in different neighborhood situations (different Wx and Wy values). We take into account the patterns respecting the periodicity criterion defined in the model (filled patterns in Fig. 6). These patterns have identical neighbors at the same Wx, Wy distance. We assume that only the nearest neighbors have a significant influence and that the other ones are far enough to neglect their effects. In Fig. 7, measured and calculated wavelengths are presented against ($Wx=Wy$) at the $O(0,0)$, $M(0,-Wy/2)$, and $N(Wx/2,0)$ points defined in Fig. 1. The reference wavelength, marked with an arrow, is in the example λ_r=1230 nm. The influence of the neighbor cells affects the three investigated points. For each point, the wavelength decreases when the dimensions of the cell (Wx,Wy) are reduced. For the M and N points, the wavelength is blue shifted as compared to the reference one. For instance, at M and N points, with $Wx=Wy$=500 μm, the blue shift is $\Delta\lambda$ =16 nm. It should be noted that the experimental and simulated points are in excellent agreement, emphasizing the validity of the model described above. As seen in this section, the proximity effects arising from neighbor cells cannot be neglected. They will naturally have an influence in the case of MQW layer integration where a high cell density is required.

VI. INTEGRATION OF MULTI-QUANTUM WELL STRUCTURES

MQW structures are nowadays widely used in optoelectronic devices. Lower threshold current for lasers, improved absorption properties based on the Stark quantum confined effect for electroabsorption modulators, or larger spectral bandwidths for semiconductor optical amplifiers (SOA) are few examples of the properties expected with these structures. Selectively grown MQW layer modeling is then a useful tool for the engineering of optoelectronic devices. The electronic states of the heterostructure are calculated within the envelope function framework developed by Bastard[22,23] and adapted for strained layers.[24] This scheme is well suited as it includes the coupling between wells and the induced

tunneling effect across the barriers. This effect cannot be neglected when the barrier becomes very thin ($\sim$5 nm), which is generally the case in the outer region of the mask. The GRE and compositional variations for the wells and barriers are calculated with Eqs. (5) and (6) and reinjected in the envelope function model, which leads to the variations of the electronic transitions in the SAG window. In selectively grown MQW structures two effects have a direct influence on the emission wavelength. The first one is the composition variation which changes both wells and barrier material band gaps. The second one is the thickness variation which changes the quantum confinement energy.

We discuss here an example of an AlGaInAs MQW structure with 10 compressive wells and 11 tensile barriers calculated and measured along the y direction ($x=0$) on mask C. Geometrical parameters of the mask are set in this example to $Wm=50$ μm, $Wo=40$ μm, and $L=1230$ μm. The cells density is high since $Wx=250$ μm and $Wy=1420$ μm, which represents an actual integration scheme configuration. On a reference unmasked sample, we deduced from HRXRD the period of the MQW (10 nm) and from combined HRXRD and PL ($\lambda_r=1365$ nm) characterizations, the respective compositions of the barriers/wells: $Al_{292}Ga_{286}In_{422}As$ / $Al_{087}Ga_{233}In_{680}As$. It should be noted that in this high-cell-density scheme, this reference material was not recovered on the wafer and was measured on another unmasked sample. Figure 8, from bottom to top, shows (a) the calculated and measured GRE of the MQW, (b) the calculated bulk heavy hole band gap for the well ($Eg_{hh}W$) and barrier ($Eg_{hh}B$), and (c) the emission wavelength (calculated and measured) arising from the fundamental transition E_1-HH_1. Similarly to the previous section, three zones I, II, and III are defined in the figure by means of vertical dashed lines, corresponding respectively to In, Al, and Ga enrichment zones. Zone II extension is very small with this mask design ($y\in[-610;-604.5]$) and is not shown for clarity. In the close vicinity of the mask (zone I), the growth rate is enhanced and both wells and barriers are enriched in indium. However, in this mask scheme, this indium enrichment is rather small. Consequently, the material band gaps of well and barrier [see Fig. 8(b)] are nearly the same as in the field region [see arrows for $Eg_{hh}W_r$ and $Eg_{hh}B_r$ in Fig. 8(b)]. In this design, Wo and Wm were selected to obtain similar GRE of indium, aluminum, and gallium species in this zone ($R_{In}\approx R_{Al}\approx R_{Ga}\neq 1$). One can easily check with Eq. (6) that when $y\in$ zone I, $C_e(0,y)\approx i_r$. Therefore in this zone, we can infer that the emission wavelength variation compared to λ_r is not due to compositional changes. The wavelength red shift [see Fig. 8(a)] is only due to the thickness effect ($R>>1$), which decreases the quantum confinement energy. In zones II and III, due to the high cell density, two combined effects are in competition. First, a non-negligible Al and Ga enrichment occurs. This composition effect increases the band gap of both wells and barriers [see Fig. 8(b)] and hence, blue shifts the emission wavelength. In addition, the reference thickness is not recovered ($R>1$ [see Fig. 8(a)]. This thickness effect decreases the quantum confinement energies and red shifts the emission wavelength. The composition effect is, however, in this present case, stronger and finally a
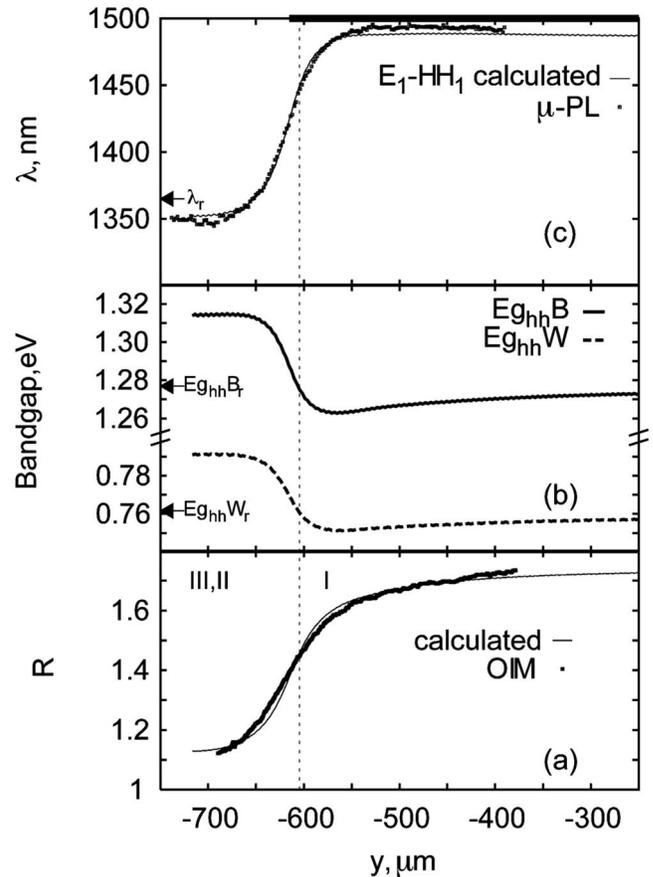

FIG. 8. Calculations and measurements (mask C) along the y axis ($x=0$) in the case of an AlGaInAs MQW structure with 10 compressive wells and 11 tensile barriers: (a) measured (OIM) and calculated growth rate enhancement (R) of the structure; (b) calculated bulk heavy holes band gap for well $Eg_{hh}W$ and barrier $Eg_{hh}B$; (c) measured (μ-PL) and calculated E_1-HH_1 transition. In this case $Wm=50$ μm, $Wo=40$ μm, $L=1230$ μm, $Wx=250$ μm, and $Wy=1420$ μm. A bold trace sketches the position of the selective mask.

small blue shift results. For instance, at point M($x=0,y=-720$), $\lambda=1350$ nm, which leads to $\Delta\lambda=(\lambda-\lambda_r)=-15$ nm. The perfect agreement found between experimental measurements and calculations for both thickness and wavelength variations validates the model.

VII. CONCLUSION

The AlGaInAs material system was thoroughly investigated in the selective area growth regime. Aluminum-based binary, ternary, and quaternary alloys were selectively grown with different mask geometries. In our growth conditions, the selectivity was perfect for each alloy of the family. Thickness profiles of InP and GaAs binaries were fitted with a VPD model in order to extract the indium and gallium characteristic diffusion lengths (D/k_s). The values found, $(D/k_s)_{Ga}=85$ μm and $(D/k_s)_{In}=10$ μm, are in qualitative agreement with previously published values. In the same way, AlAs binary alloy was measured to extract the aluminum diffusion length value. We found, in our growth conditions $(D/k_s)_{Al}=50$ μm, an intermediate value between that of indium and gallium. Computational analysis with a systematic comparison with experiments was conducted to evaluate the growth

rate enhancement and compositional variations of ternary and quaternary alloys. For these alloys, a simple linear dependence of the growth rate enhancement with the involved binaries was assumed. This perfectly matches our experiments and previous reports in the GaInAsP material system. We also brought new insights on Al and Ga long-range effects in the high-cell-density configurations. These effects were investigated with the model which including periodicity of the SAG cell as a boundary condition. A special mask, designed with varying periodicity of the SAG cell, was also investigated and showed that high-density integration schemes induce important proximity effects that cannot be neglected. For instance, we showed that blue/red shift of the wavelength and tensile/compressive shift of the biaxial strain, as compared to the field region reference, depend on the position (x,y) in the cell and on its periodicity. Highly resolved μ-photoluminescence confirmed the validity of these results. Finally, a MQW structure was selectively grown and analyzed with a specific mask design corresponding to a real integration scheme. In these integrated structures, the high cell density is a requirement and important proximity effects naturally occur between the different masks. We demonstrated that the VPD model is able to predict with a high accuracy the selective area growth effects for any AlGaInAs structure, including complex stacking like MQW layers. This study offers a very attractive tool for complex and precise engineering of SAG optoelectronic integrated devices.

[1] J. Binsma, P. Thijs, T. VanDongen, E. Jansen, A. Staring, G. Van-DenHoven, and L. Tiemeijer, IEICE Trans. Electron. **E80**, C675 (1997).

[2] R. J. Deri, C. Caneau, E. Colas, L. M. Schiavone, N. C. Andreadakis, G. H. Song, and E. C. M. Pennings, Appl. Phys. Lett. **61**, 952 (1992).

[3] W. T. Tsang, J. E. Johnson, P. A. Morton, T. Tanbun-Ek, S. N. G. Chu, and W. D. Johnston, IEEE MTT-S Int. Microwave Symp. Dig. **1995**, 247.

[4] D. Delprat, A. Ramdane, L. Silvestre, A. Ougazzaden, F. Delorme, and S. Slempkes, IEEE Photon. Technol. Lett. **9**, 898 (1997).

[5] J. E. Johnson, L. J. Ketelsen, J. A. Grenko, S. K. Sputz, J. Vandenberg, M. W. Focht, D. V. Stampone, L. J. Petitnicolas, L. E. Smith, K. G. Glogovsky, G. J. Przybylek, S. N. G. Chu, J. L. Lentz, N. N. Tzafaras, L. C. Luther, T. L. Pernell, F. S. Walters, D. M. Romero, J. M. Freund, C. L. Reynolds, L. A. Gruezke, R. People, and M. A. Alam, IEEE J. Sel. Top. Quantum Electron. **6**(1),19 (2000).

[6] L. Hou, H. Zhu, F. Zhou, L. Wang, J. Bian, and W. Wang, Semicond. Sci. Technol. **20**, 912 (2005).

[7] H. Hatakeyama, K. Kudo, Y. Yokoyama, K. Naniwae, and T. Sasaki, IEEE J. Sel. Top. Quantum Electron. **8**, 1341 (2002).

[8] S. Sudo, Y. Yokoyama, T. Nakazaki, K. Mori, K. Kudo, M. Yamaguchi, and T. Sasaki, J. Cryst. Growth **221**, 189 (2000).

[9] C. Caneau, R. Bhat, C. C. Chang, K. Kash, and M. A. Koza, J. Cryst. Growth **132**, 364 (1993).

[10] R. Westphalen, B. Elsner, M. Maassen, O. Kayser, K. Heime, and P. Balk, J. Cryst. Growth **125**, 347 (1992).

[11] M.-S. Kim, C. Caneau, E. Colas, and R. Bhat, J. Cryst. Growth **123**, 69 (1992).

[12] M. Gibbon, J. P. Stagg, C. G. Cureton, E. J. Trush, C. J. Jones, R. E. Mallard, R. E. Pritchard, N. Collis, and A. Chew, Semicond. Sci. Technol. **8**, 998 (1993).

[13] M. A. Alam, R. People, E. Isaacs, C. Y. Kim, K. Evans-Lutterodt, T. Siegrist, T. L. Pernell, J. Vandenberg, S. K. Sputz, S. N. G. Chu, D. V. Lang, L. Smith, and M. S. Hybertsen, Appl. Phys. Lett. **74**, 2617 (1999).

[14] T. Shioda, T. Doi, A. A. Amin, X. Song, and M. Sugiyama, Thin Solid Films, **498**, 174 (2006).

[15] A. A. Sirenko, A. Kazimirov, R. Huang, D. H. Bilderback, S. M. O'Malley, V. K. Gupta, K. Bacher, L .J. P. Ketelsen, and A. Ougazzaden, J. Appl. Phys., **97**, 063512 (2005).

[16] A. A. Sirenko, A. Kazimirov, A. Ougazzaden, S. M. O'Malley, D. H. Bilderback, Z. H. Cai, B. Lai, R. Huang, V. K. Gupta, M. Chien, and S. N. G. Chu, Appl. Phys. Lett., **88**, 081111 (2006).

[17] T. Tsuchiya, J. Shimizu, M. Shirai, and M. Aoki, J. Cryst. Growth, **276**, 439 (2005).

[18] W. Feng, W. Wang, H. Zhu, L. Zhao, L. Hou, and J. Pan, Semicond. Sci. Technol. **20**, 1083 (2005).

[19] J. Décobert, N. Lagay, C. Cuisin, B. Dagens, B. Thedrez, and F. Laruelle, J. Cryst. Growth **272**, 543 (2004).

[20] J. Décobert, N. Dupuis, P.-Y. Lagrée, N. Lagay, A. Ramdane, A. Ougazzaden, F. Poingt, C. Cuisin, and C. Kazmierski, J. Cryst. Growth **298**, 28 (2007).

[21] M. A. Jones, M. L. Osowski, R. M. Lammert, J. A. Dantzig, and J. J. Coleman, J. Electron. Mater. **24**, 1631 (1995).

[22] G. Bastard, Phys. Rev. B **24**, 5693 (1981).

[23] G. Bastard, *Wave mechanics applied to semiconductor heterostructures* (Les éditions de physique, Les Ulis, 1988).

[24] J. Y. Marzin, *Heterojunctions and semiconductor superlattices*, in Strained Superlattices, edited by G. Allan, G. Bastard, N. Boccara, M. Lannoo, and M. Voos (Springer, Berlin, 1986).